Short communication

Antimony nanoparticles anchored in three-dimensional carbon network as promising sodium-ion battery anode
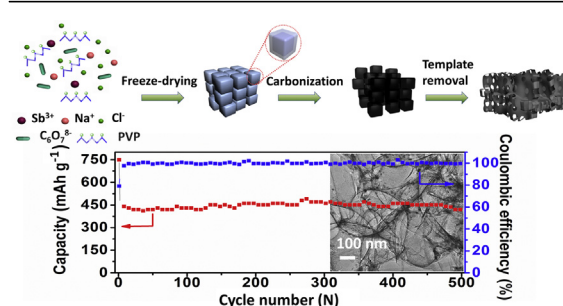
Wen Luo [1], Pengfei Zhang [1], Xuanpeng Wang, Qidong Li, Yifan Dong, Jingchen Hua, Liang Zhou, Liqiang Mai*

State Key Laboratory of Advanced Technology for Materials Synthesis and Processing, Wuhan University of Technology, Wuhan 430070, PR China

HIGHLIGHTS

- SbNPs@3D-C was achieved by template-assisted freeze-drying and carbonization.
- SbNPs@3D-C showed nano-sized Sb particles anchored in 3D carbon network structure.
- Long-life performance (500 cycles) and superior rate ability were demonstrated.
- NaCl template-assisted strategy combined with freeze-drying can be widely extended.

GRAPHICAL ABSTRACT

ARTICLE INFO

ABSTRACT

A novel composite with antimony (Sb) nanoparticles anchored in three-dimensional carbon network (denoted as SbNPs@3D-C) is successfully synthesized *via* a NaCl template-assisted self-assembly strategy, followed by freeze-drying and one-step *in-situ* carbonization. The three-dimensional interconnected macroporous carbon framework can not only stabilize the architecture and buffer the volume expansion for Sb nanoparticles, but also provide high electrical conductivity for the whole electrode. Consequently, as a sodium-ion battery anode, the SbNPs@3D-C delivers a high reversible capacity (456 mAh g^{-1} at 100 mA g^{-1}), stable cycling performance (94.3% capacity retention after 500 cycles at 100 mA g^{-1}) as well as superior rate capability (270 mAh g^{-1} at 2000 mA g^{-1}). When compared with commercial Sb particles, the SbNPs@3D-C exhibits dramatically enhanced electrochemical performance. Free from expensive template sources and complex manipulation, this work might shed some light on the synthesis of low-cost and high-performance materials for the next "beyond lithium" battery generation.

1. Introduction

Widespread implementation of advanced energy-storage systems requires high efficiency, low cost, and sustainability.

Rechargeable lithium-ion batteries (LIBs) are one of the most successful energy storage devices, which have rapidly penetrated into everyday life [1–4]. However, the utilization of LIBs for electrical grid is a controversial plan due to the limited lithium resource. Sodium, which locates below lithium in the periodic table, shares similar chemical properties in many aspects. In addition, it is abundant and low-cost. Thus, sodium is an ideal alternative to lithium in energy storage systems [5–8]. Over the past decades, many layered oxides [9], oxides [10], and polyanionic compounds

[11] have been intensively investigated as cathode materials for sodium-ion batteries (SIBs). With regard to anode materials, the pristine graphite has a very low capacity when used as a SIBs anode because of insufficient interlayer spacing [12,13]. Various carbonaceous materials, including soft [14] and hard carbon [15], hollow carbon nanospheres [16], hollow carbon nanowires [17], carbon nanosheets [18], reduced graphene oxides [19,20] have been investigated. Nevertheless most of these carbonaceous materials possess low specific capacities less than 300 mAh g^{-1}, for instance, the hard carbon C1600 [15] delivers a reversible capacity of 290 mAh g^{-1} at a specific current of 20 mA g^{-1}; the hollow carbon nanospheres [16] exhibit a reversible capacity of 200 mAh g^{-1} at a specific current of 50 mA g^{-1}, which cannot meet the ever-increasing demand for high-capacity energy storage devices. Moreover, most intercalation type anodes display high working potentials, resulting in low energy density [21]. Therefore, to improve the overall performance of SIBs, the pursuit of new anode materials with high capacity and long life remains a great challenge.

Recently, antimony has been investigated as a promising anode due to its high specific capacity of 660 mAh g^{-1} when fully sodiated to Na$_3$Sb: $3Na^+ + Sb + 3e^- \leftrightarrow Na_3Sb$ [22]. Nevertheless, the large volume change during sodium ion insertion/extraction causes active material fracture and loss of electrical contact, resulting in poor electrochemical performance. Previous reports on Sb anode for SIBs mainly include mechanically milled Sb/C composites [23], reduced graphene oxide/Sb particles [24], electrospun Sb/C nanowires [25,26], Sb/N-rich carbon nanosheets [27], hollow Sb particles [28], monodisperse Sb nanoparticles [29], mechanically milled Sb/MWCNT composites [30], one-dimensional Sb@C [31] etc. For example, Cao et al. [26] reported the synthesis of Sb/C nanofibers with a high reversible capacity of 631 mAh g^{-1} and an impressive capacity retention of 90% for 400 cycles. Hu et al. [32] reported the assembly of full-cell with Sb/rGO anode and Na$_3$V$_2$(PO$_4$)$_3$/rGO cathode. However, most of the above-mentioned strategies are complicated and time-consuming. Besides, the electrochemical performances of the resulted anode materials are not very satisfactory. In this regard, a direct synthesis route for Sb-based anodes with high performance is urgently desired.

Currently, three-dimensional conductive nanostructures have become a rapidly growing field of energy storage research because of their large surface area, continuous interconnected network, and excellent interface [33,34]. On the other hand, reducing the particle size from bulk to nanoscale can effectively enhance electrochemical reaction kinetics [35]. By combining nanosized active materials with three-dimensional network, some encouraging advances have been achieved in lithium-ion batteries [36] and supercapacitors [37]. However, conventional template-assisted methods for macroporous three-dimensional construction are complex. First, the templates should be concisely modified to endow themselves with compatibility between core and shell. Then, most of the template-removal processes are often energy-consuming or danger-risking. Herein we develop a novel NaCl template-assisted self-assembly strategy followed by freeze-drying and carbonization to construct SbNPs@3D-C composites. The synthesized SbNPs@3D-C exhibits long cycling stability and improved rate performance. We believe this work might shed some light on the synthesis of high-performance hybrid electrode materials for future low-cost, large-scale energy storage system.

2. Results and discussion

Fig. 1 schematically illustrates the synthesis procedure. In the first step (step I), SbCl$_3$, citric acid, polyvinyl pyrrolidone (PVP), and NaCl were dissolved in water, frozen by liquid nitrogen, and subjected to freeze-drying. Herein, SbCl$_3$ was used as the Sb precursor. Citric acid, a weak organic acid with three carboxyl groups, coordinated with and inhibited the hydrolysis of Sb^{3+}. PVP, an amphiphilic and water-soluble polymer [38], acted as the capping agent to confine the size and morphology of NaCl particles. It is well known that NaCl has a face-centered cubic (FCC) crystal structure [39]. During freeze-drying, the NaCl grew into cubes, which further self-assembled into three-dimensional structure and acted as the template for the carbon network. Meanwhile, the in-situ formed SbCl$_3$/citric acid/PVP composite coated evenly on the surface of the NaCl template. In step II, the as-obtained sponge-like sample after freeze-drying was ground and carbonized. Upon heating in H$_2$/Ar, the PVP and citric acid were pyrolyzed, forming a three-dimensional interconnected carbon network. Meanwhile, the Sb^{3+} was reduced to Sb nanoparticles firmly anchored in the three-dimensional carbon network. Finally (step III), the NaCl template was thoroughly removed by deionized water and pure SbNPs@3D-C was obtained.

X-ray diffraction (XRD) is used to study the crystalline structure of the obtained samples. As depicted in Fig. 2a, the diffraction peaks can be indexed to crystalline Sb (space group: $R\overline{3}m$, a = b = 0.4307 nm, c = 1.1273 nm, JCPDS: 01-071-1173), attesting the complete reduction of Sb^{3+} to metallic Sb through the annealing in H$_2$/Ar. The sharp diffraction peaks verify that the Sb is well crystallized. According to Scherrer equation, the average crystallite size of Sb is calculated to be 16.4 nm. Due to the intense diffraction peaks of Sb, the weak diffraction signal of carbon matrix can be hardly detected (Fig. S1).

SbNPs@3D-C composites are further evaluated by Raman spectroscopy to confirm carbon material (Fig. 2b). Raman shifts around 1350 cm^{-1} and 1590 cm^{-1} correspond to the D and G band of carbon, respectively. The I$_D$ to I$_G$ ratio of SbNPs@3D-C (~1.02) is different from that of 3D-C (~0.99). The reasonable interpretation is that metallic Sb nanoparticles might affect the growth of graphitic carbon [31].

Thermogravimetric analysis (TGA) is performed to determine the content of Sb in SbNPs@3D-C composite. As manifested in Fig. 2c, approximately 3.6 wt% weight loss at around 100 °C corresponds to the loss of adsorbed water in the sample. The weight loss at around 460 °C is mainly caused by the combustion of carbon, and the weight gain after 495 °C might be attributed to the oxidation of Sb [26]. Accordingly, the mass ratio of Sb in the composite is determined to be 31.2 wt%.

Fig. 3a–f display the scanning electron microscopy (SEM) images of the samples at each independent state in sequence. The mixture obtained after the freeze-drying exhibits an aggregated cubic morphology, indicating the SbCl$_3$/citric acid/PVP are evenly coated on the surface of the NaCl cubes (Fig. 3a). Benefiting from the confining effect of PVP, the size of the NaCl cubic particles are properly controlled to be around 1 μm. When viewed in details (Fig. 3b), it can be found that the cubic particles are well-interconnected to each other. When other surfactants/polymers are used to replace PVP, either cubic particles with large size deviation or irregular shaped particles are obtained (Fig. S2), demonstrating the crucial role of PVP in the synthesis. During carbonization, the original morphology of the uniform, micrometer-sized, and interconnected cubic particles can be generally maintained with the assistance of the NaCl template. However, the particles aggregate more closely and tightly than before and the particle size is shrank from micrometer to submicrometer (Fig. 3c). High magnification SEM image of the carbonized sample (Fig. 3d) shows slightly collapsed facets, which is caused by the shrinkage towards the NaCl core during heat treatment. After a simple washing process, the NaCl template can be thoroughly removed and the SbNPs@3D-C composite can be
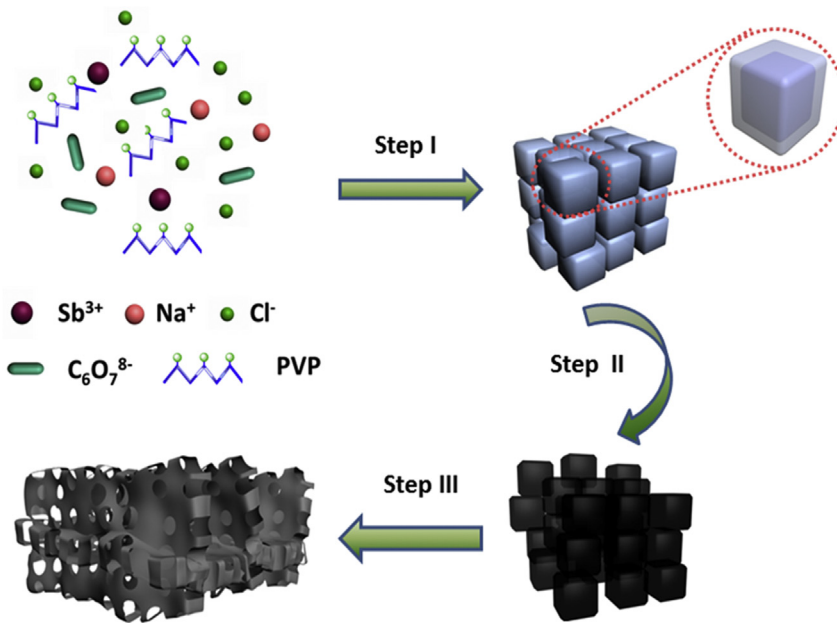
Fig. 1. Schematic illustration of the synthesis procedure. Step I: freeze drying; step II: carbonization; step III: template removal.
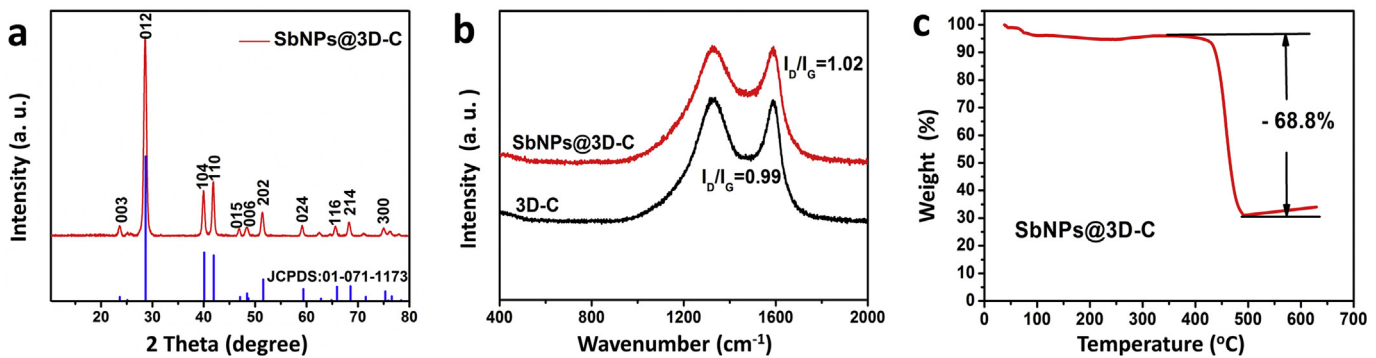

Fig. 2. (a) XRD pattern of the SbNPs@3D-C. (b) Raman spectra of the SbNPs@3D-C and 3D-C. (c) TGA profile of the SbNPs@3D-C.

successfully realized (Fig. 3e, f). The SbNPs@3D-C shows a three-dimensional macroporous structure with interconnected backbone. No obvious Sb particles can be observed on the surface, suggesting that the Sb nanoparticles might be embedded in the carbon matrix. To further explore the microstructure of SbNPs@3D-C, transmission electron microscopy (TEM) is implemented. According to Fig. 3g, uniform Sb nanoparticles are dispersedly embedded in the interconnected carbon network. The size of the Sb nanoparticles is in the range of 10–20 nm, in agreement with the XRD result. Under high-resolution TEM (HRTEM), as shown in Fig. 3f, the lattice fringe with a spacing of 0.31 nm is clearly observed, which can be attributed to the (012) plane of rhombohedral Sb. All the above characterizations confirm the unique composite structure of Sb nanoparticles anchored in three-dimensional carbon network.

The electrochemical performances of SbNPs@3D-C are shown in Fig. 4. It should be mentioned that the acetylene black provides a very low sodiation capacity (Fig. S3, Fig. S4). Thus all the capacities given in this study are mainly contributed from the active material (defined as SbNPs@3D-C). Fig. 4a reveals the cyclic voltammograms (CV) of the SbNPs@3D-C at a scan rate of 0.1 mV s^{-1} in the potential window of 0.01–3.0 V vs. Na$^+$/Na. In the first cycle, the cathodic

peak at 0.19 V can be ascribed to the conversion of crystalline Sb to Na$_3$Sb and the irreversible decomposition of the electrolyte [28,40]; the anodic shape peak at 1.02 V can be attributed to the phase transition from Na$_3$Sb to Sb. Additionally, in the first anodic cycle, the oxidation peak at about 2.88 V should be associated to the presence of Cu$_x$O$_y$ which is probably originated when slurry-loaded Cu foils are dried in the air condition [41]. Since this peak disappears after the first cycle and, its contribution to the overall capacity is negligible, Cu$_x$O$_y$ should be considered as an active material impurity. Moreover, as already reported [42], the electrolyte used during the electrochemical tests (1 M NaClO$_4$ dissolved in ethylene carbonate (EC)/dimethyl carbonate (DMC) (1:1 by volume) with 5% fluoroethylene carbonate (FEC) additive) hardly decomposes at 2.88 V, thus excluding any kind of electrolyte decomposition processes. In the second and third cycles, two pairs of reversible redox peaks at 0.33/1.12 V and 0.19/1.01 V can be observed, which are ascribed to the two-step alloying reaction of Sb to Na$_x$Sb and Na$_3$Sb [23]. The curves of the second and third cycle almost overlap, confirming the good reversibility of the SbNPs@3D-C electrode. The big difference between the first and following cycles is mainly caused by the irreversible electrolyte decomposition and formation of solid electrolyte interphase (SEI) layer
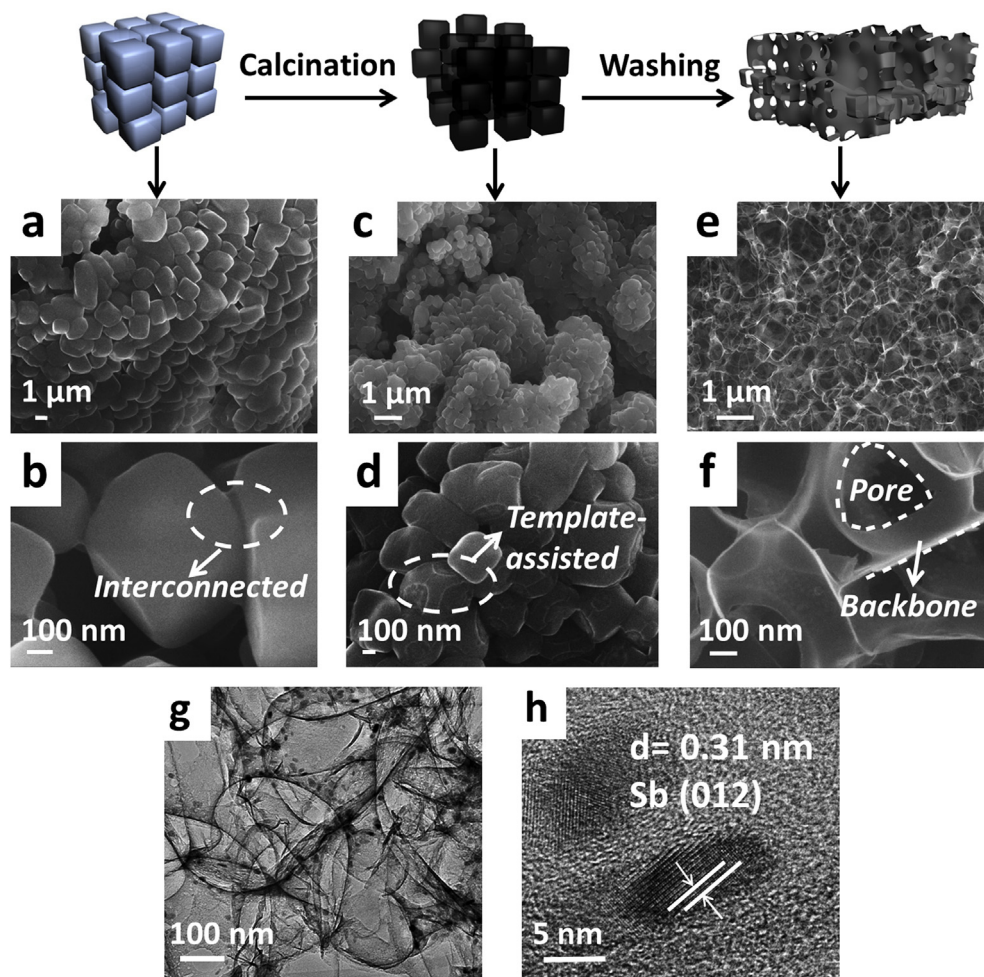
Fig. 3. SEM & TEM characterization and schematic illustration of the samples at different states. (a, b) SEM images of the SbCl₃/citric acid/PVP/NaCl composite particles after freeze-drying; (c, d) SEM images of SbNPs@3D-C@NaCl; (e, f) SEM images of SbNPs@3D-C; (g) TEM image of SbNPs@3D-C; (h) HRTEM image of SbNPs@3D-C.

[43–45].

Fig. 4b manifests representative galvanostatic discharge–charge profiles of SbNPs@3D-C at a specific current of 100 mA g^{-1}. The first discharge and charge capacities are 790 and 625 mAh g^{-1}, corresponding to a relatively low initial Coulombic efficiency of 79.1%. The irreversible capacity loss is due to the formation of SEI. As for the 250th and 500th cycle, small capacity loss occurred externalizing the stable cycling performance of SbNPs@3D-C. Fig. 4c further evaluates the long life performance of SbNPs@3D-C, when cycling at a specific current of 100 mA g^{-1}, an inevitable capacity loss occurred after first cycle, which was in good agreement with the above CV curve. For second cycle, a capacity of 456 mAh g^{-1} was achieved and still retained 430 mAh g^{-1} after 500 cycles, corresponding to capacity retention of 94.3% (calculating based on second discharge capacity and 500th discharge capacity). Moreover, except the initial cycle, the Coulombic efficiency maintained above 99.0% during the subsequent cycles (Fig. S5), declaring a facile and efficient alloying/dealloying of sodium ions in the anode. It is well known Sb electrode will not exhibit impressive electrochemical performance without fluoroethylene carbonate (FEC) additive in the electrolyte [23]. By comparison, the SbNPs@3D-C delivered an unstable and low capacity in the FEC free electrolyte. Fig. 4d exhibits the cycle performance of SbNPs@3D-C under a high specific current. Impressively, when charged and discharged at 2000 mA g^{-1}, the reversible capacity can reach 270 mAh g^{-1} and it

still achieved long life performance with 85% of its initial capacity retained after 300 cycles. In contrast, under this high specific current, the SbNPs@3D-C can cycle in the first 50 cycles and then only provide a capacity of ~30 mAh g^{-1} in the FEC free electrolyte. The cell also represented a high Coulombic efficiency for the whole cycling process (Fig. S6), which corroborated the great cycling stability and excellent long life performance of SbNPs@3D-C.

Rate performance of as-synthesized SbNPs@3D-C was also investigated. As comparison electrodes, commercial Sb powder without any treatment (Fig. S7) and 3D-C were also fabricated into cell and tested under the same condition. As shown in Fig. 4e, the electrode made from SbNPs@3D-C demonstrated dramatically improved rate capability compared to the commercial Sb powder. The SbNPs@3D-C electrode displayed an average capacity of 515, 478, 429, 360, 278 and 200 mAh g^{-1} at the specific current of 50, 100, 200, 400, 800 and 1600 mA g^{-1}, respectively. Remarkably, when the cell was discharged at 50 mA g^{-1} again, a high capacity of 468 mAh g^{-1} can be still obtained, suggesting the superior capacity reversibility of SbNPs@3D-C electrode. In contrast, commercial Sb powder and 3D-C (Fig. S8) can offer considerable capacity for the first few cycles, whereas, with the specific current increasing, they only provided negligible capacity during the subsequent cycling process. This result forcefully declares the excellent performance of our three-dimensional Sb nanoparticles anchored in interconnected carbon network composite in sodium storage system.
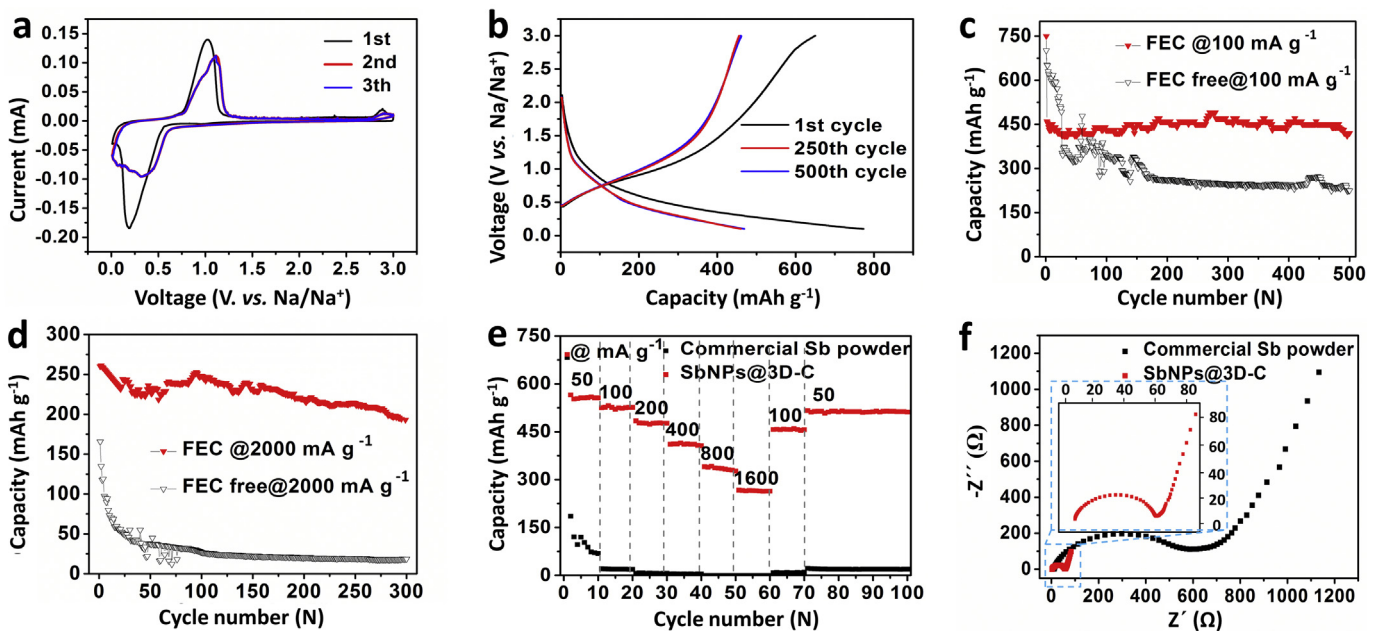
Fig. 4. Electrochemical characterizations and cell performances of SbNPs@3D-C electrode. (a) Cyclic voltammetry of SbNPs@3D-C between 0.01 and 3 V at a scanning rate of 0.1 mV s^{-1}. (b) Charge and discharge curves SbNPs@3D-C at a specific current of 100 mA g^{-1}. (c) Cycle performance of SbNPs@3D-C electrode at a specific current of 100 mA g^{-1} with and without 5% FEC additive. (d) Cycle performance of SbNPs@3D-C electrode at a specific current of 2000 mA g^{-1} with and without 5% FEC additive. (e) Rate performance of SbNPs@3D-C and commercial Sb powder electrode. (f) EIS spectra of SbNPs@3D-C and commercial Sb electrode before cycling.

Electrochemical Impedance Spectroscopy (EIS) measurements of SbNPs@3D-C electrode and commercial Sb powder electrode were employed respectively before cycling. As can be seen in Fig. 4f, the EIS plots of both electrodes were constituted by a single depressed semicircle in the high frequency region and an inclined line at low frequency. It is well known that the semicircle at the high frequency represents the SEI resistance and contact resistance, while the inclined line at the low frequency can be attributed to the Warburg impedance related to sodium ion diffusion in the electrode [17]. From Fig. 4f, it is clear that the semicircle diameter of SbNPs@3D-C is significantly smaller than that of Sb commercial powder. That is to say, the contact and charge-transfer resistance of the SbNPs@3D-C is significantly smaller than those of the commercial Sb powder.

The morphological and structural changes of the SbNPs@3D-C after charge/discharge are also explored. Fig. S9 shows the SEM and elemental mapping results of the SbNPs@3D-C after 100 cycles. It is clearly observed that the macroporous three-dimensional architecture does not change considerably (Fig. S9a), while the surface of the carbon network becomes thicker and rougher compared to the SbNPs@3D-C before cycling (Fig. S9b). The elemental mappings of carbon and antimony confirm that Sb particles are well restricted within the carbon network even after 100 charge–discharge cycles. Besides, the homogeneous distribution of sodium indicates the formation of a uniform SEI film on the surface of the SbNPs@3D-C, in agreement with previous report [30]. These results demonstrate that the unique structure of SbNPs@3D-C can efficiently accommodate the volume expansion and maintain its structural integrity, leading to excellent cycling and rate performance.

The above electrochemical performances of SbNPs@3D-C positively validate the superiority of three-dimensional hybrid structure. The excellent sodium storage performances can be ascribed to the following structural benefits. First, the Sb nanoparticles are uniformly embedded in the robust carbon network. This unique feature not only buffers the volume expansion but also prevents the aggregation and pulverization of Sb, leading to excellent cycling stability. Second, the three-dimensional interconnected carbon network provides a highly conductive pathway for electron diffusion, contributing to the high rate capability. Third, the three-dimensional macroporous structure allows the access of sodium ions from various directions, further boosting the rate performance.

3. Conclusion

In summary, a novel composite with Sb nanoparticles anchored in three-dimensional carbon network has been successfully synthesized through a template-assisted self-assembly method, followed by freeze-drying and carbonization. When used as the anode material for sodium-ion batteries, the resulting composite delivers a high reversible capacity (456 mAh g^{-1} at 100 mA g^{-1}), stable cycling performance (94.3% capacity retention after 500 cycles at 100 mA g^{-1}) as well as superior rate capability (270 mAh g^{-1} at 2000 mA g^{-1}). The excellent electrochemical performances can be attributed to the unique structural features such as the Sb nanoparticles uniformly anchored in the robust matrix, highly conductive interconnected carbon network, and three-dimensional macroporous structure. At last, different from the conventional template methods, the introduction of inexpensive NaCl template and facile template-removal process in water show great potential in controllable synthesize for novel architectures. It is expected that this strategy would be extended to the preparation of other nanostructures by proper experimental design and optimization.

Appendix A. Supplementary data

Supplementary data related to this article can be found at http://dx.doi.org/10.1016/j.jpowsour.2015.11.047.

References

[1] B. Dunn, H. Kamath, J.-M. Tarascon, Science 334 (2011) 928—935.
[2] L. Mai, X. Tian, X. Xu, L. Chang, L. Xu, Chem. Rev. 114 (2014) 11828—11862.
[3] S.W. Kim, D.H. Seo, X. Ma, G. Ceder, K. Kang, Adv. Energy Mater. 2 (2012) 710—721.
[4] B. Scrosati, J. Garche, J. Power Sources 195 (2010) 2419—2430.
[5] V. Palomares, P. Serras, I. Villaluenga, K.B. Hueso, J. Carretero-González, T. Rojo, Energy Environ. Sci. 5 (2012) 5884—5901.
[6] M.D. Slater, D. Kim, E. Lee, C.S. Johnson, Adv. Funct. Mater. 23 (2013) 947—958.
[7] V. Palomares, M. Casas-Cabanas, E. Castillo-Martínez, M.H. Han, T. Rojo, Energy Environ. Sci. 6 (2013) 2312—2337.
[8] S.Y. Hong, Y. Kim, Y. Park, A. Choi, N.-S. Choi, K.T. Lee, Energy Environ. Sci. 6 (2013) 2067—2081.
[9] N. Yabuuchi, K. Kubota, M. Dahbi, S. Komaba, Chem. Rev. 114 (2014) 11636—11682.
[10] Y. Dong, S. Li, K. Zhao, C. Han, W. Chen, B. Wang, L. Wang, B. Xu, Q. Wei, L. Zhang, Energy Environ. Sci. 8 (2015) 1267—1275.
[11] S. Li, Y. Dong, L. Xu, X. Xu, L. He, L. Mai, Adv. Mater. 26 (2014) 3545—3553.
[12] Y. Wen, K. He, Y. Zhu, F. Han, Y. Xu, I. Matsuda, Y. Ishii, J. Cumings, C. Wang, Nat. Commun. 5 (2014) 4033.
[13] Z. Zhu, F. Cheng, Z. Hu, Z. Niu, J. Chen, J. Power Sources 293 (2015) 626—634.
[14] D. Stevens, J. Dahn, J. Electrochem. Soc. 148 (2001) A803—A811.
[15] J. Zhao, L. Zhao, K. Chihara, S. Okada, J.-I. Yamaki, S. Matsumoto, S. Kuze, K. Nakane, J. Power Sources 244 (2013) 752—757.
[16] K. Tang, L. Fu, R.J. White, L. Yu, M.M. Titirici, M. Antonietti, J. Maier, Adv. Energy Mater. 2 (2012) 873—877.
[17] Y. Cao, L. Xiao, M.L. Sushko, W. Wang, B. Schwenzer, J. Xiao, Z. Nie, L.V. Saraf, Z. Yang, J. Liu, Nano Lett. 12 (2012) 3783—3787.
[18] J. Ding, H. Wang, Z. Li, A. Kohandehghan, K. Cui, Z. Xu, B. Zahiri, X. Tan, E.M. Lotfabad, B.C. Olsen, ACS nano 7 (2013) 11004—11015.
[19] R. Raccichini, A. Varzi, S. Passerini, B. Scrosati, Nat. Mater. 14 (2015) 271—279.
[20] Y.-X. Wang, S.-L. Chou, H.-K. Liu, S.-X. Dou, Carbon 57 (2013) 202—208.
[21] P. Senguttuvan, G.l. Rousse, V. Seznec, J.-M. Tarascon, M.R. Palacin, Chem. Mater. 23 (2011) 4109—4111.
[22] A. Darwiche, C. Marino, M.T. Sougrati, B. Fraisse, L. Stievano, L. Monconduit, J. Am. Chem. Soc. 134 (2012) 20805—20811.
[23] J. Qian, Y. Chen, L. Wu, Y. Cao, X. Ai, H. Yang, Chem. Commun. 48 (2012) 7070—7072.
[24] C. Nithya, S. Gopukumar, J. Mater. Chem. A 2 (2014) 10516—10525.
[25] Y. Zhu, X. Han, Y. Xu, Y. Liu, S. Zheng, K. Xu, L. Hu, C. Wang, ACS nano 7 (2013) 6378—6386.
[26] L. Wu, X. Hu, J. Qian, F. Pei, F. Wu, R. Mao, X. Ai, H. Yang, Y. Cao, Energy & Environ. Sci. 7 (2014) 323—328.
[27] X. Zhou, Y. Zhong, M. Yang, M. Hu, J. Wei, Z. Zhou, Chem. Commun. 50 (2014) 12888—12891.
[28] H. Hou, M. Jing, Y. Yang, Y. Zhu, L. Fang, W. Song, C. Pan, X. Yang, X. Ji, ACS Appl. Mater. interfaces 6 (2014) 16189—16196.
[29] M. He, K. Kravchyk, M. Walter, M.V. Kovalenko, Nano Lett. 14 (2014) 1255—1262.
[30] X. Zhou, Z. Dai, J. Bao, Y.-G. Guo, J. Mater. Chem. A 1 (2013) 13727—13731.
[31] W. Luo, S. Lorger, B. Wang, C. Bommier, X. Ji, Chem. Commun. 50 (2014) 5435—5437.
[32] W. Zhang, Y. Liu, C. Chen, Z. Li, Y. Huang, X. Hu, Small 11 (2015) 3822—3829.
[33] Y. Zhao, B. Liu, L. Pan, G. Yu, Energy Environ. Sci. 6 (2013) 2856—2870.
[34] J.H. Pikul, H.G. Zhang, J. Cho, P.V. Braun, W.P. King, Nat. Commun. 4 (2013) 1732.
[35] H. Liu, F.C. Strobridge, O.J. Borkiewicz, K.M. Wiaderek, K.W. Chapman, P.J. Chupas, C.P. Grey, Science 344 (2014) 1252817.
[36] H. Zhang, P.V. Braun, Nano Lett. 12 (2012) 2778—2783.
[37] X.-C. Dong, H. Xu, X.-W. Wang, Y.-X. Huang, M.B. Chan-Park, H. Zhang, L.-H. Wang, W. Huang, P. Chen, ACS nano 6 (2012) 3206—3213.
[38] T. Sun, H. King, Macromolecules 29 (1996) 3175—3181.
[39] D. Chakraborty, G. Patey, J. Phys. Chem. Lett. 4 (2013) 573—578.
[40] L. Baggetto, P. Ganesh, C.-N. Sun, R.A. Meisner, T.A. Zawodzinski, G.M. Veith, J. Mater. Chem. A 1 (2013) 7985—7994.
[41] S. Venkatachalam, H. Zhu, C. Masarapu, K. Hung, Z. Liu, K. Suenaga, B. Wei, ACS nano 3 (2009) 2177—2184.
[42] A. Ponrouch, E. Marchante, M. Courty, J.-M. Tarascon, M.R. Palacin, Energy Environ. Sci. 5 (2012) 8572—8583.
[43] L. Fu, K. Tang, K. Song, P.A. van Aken, Y. Yu, J. Maier, Nanoscale 6 (2014) 1384—1389.
[44] Y. Yu, L. Gu, C. Wang, A. Dhanabalan, P.A. van Aken, J. Maier, Angew. Chem. Int. Ed. 48 (2009) 6485—6489.
[45] Y. Xu, J. Guo, C. Wang, J. Mater. Chem. 22 (2012) 9562—9567.